

Photoactive hourglass-type $M\{P_4Mo_6\}_2$ networks for efficient removal of hexavalent chromium

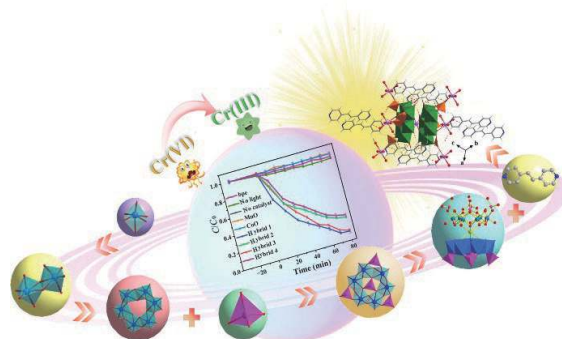
Xiao-Yu Yin, Hao-Xue Bi, Hao Song, Jing-Yan He, Yuan-Yuan Ma , Ting-Ting Fang, and Zhan-Gang Han 

Hebei Key Laboratory of Organic Functional Molecules, National Demonstration Center for Experimental Chemistry Education, Hebei Key Laboratory of Inorganic Nanomaterials, College of Chemistry and Materials Science, Hebei Normal University, Shijiazhuang 050024, China

 Cite This: *Polyoxometalates*, 2023, 2, 9140027

 Read Online

ABSTRACT: The exploration of high-efficiency photocatalysts to drive the conversion of highly toxic heavy metal hexavalent chromium (Cr(VI)) in wastewater to low-toxic trivalent chromium (Cr(III)) is of great significance for purifying water that contains emerging contaminants. Herein, four hourglass-type phosphomolybdate-based hybrid networks— $(H_2bpe)_2[M(H_2O)_3]_2\{M[P_4Mo_6O_{31}H_7]_2\} \cdot 8H_2O$ ($M = Mn$ for **1**, Co for **2**) and $(Hbpe)(H_2O)_3Na[M(H_2O)_3]_2\{M[P_4Mo_6O_{31}H_7]_2\} \cdot 9H_2O$ ($M = Mn$ for **3**, Co for **4**; $\{M[P_4Mo_6O_{31}H_7]_2\}^{8-}$ (abbr. $M\{P_4Mo_6\}_2$); $bpe = 1,2$ -di(4-pyridyl) ethylene)—were hydrothermally synthesized as heterogeneous photocatalysts for Cr(VI) reduction. A structural analysis showed that the four hybrids **1–4** exhibited two-dimensional inorganic sheet-like structures with a 3,6-connected *kfd* topology built of hourglass phosphomolybdate clusters having different central metal ions, which further interacted with organic *bpe* cations via abundant hydrogen-bonding interactions to extend the structure to a three-dimensional (3D) supramolecular network. The four hybrids displayed excellent redox properties and wide visible-light absorption. When used as heterogeneous photocatalysts, hybrids **1–4** exhibited excellent photocatalytic activity for Cr(VI) reduction under 10 W white light irradiation, with reduction rates of 91% for **1**, 74% for **2**, 90% for **3**, and 71% for **4**, respectively, within 80 min. The Cr(VI) reduction reaction over hybrids **1–4** followed the pseudo first-order kinetics model with reaction rate constants k of 0.0237 min^{-1} for **1**, 0.0143 min^{-1} for **2**, 0.0221 min^{-1} for **3** and 0.0134 min^{-1} for **4**, respectively. The $Mn\{P_4Mo_6\}_2$ -based hybrids **1** and **3** showed better photocatalytic performance than the $Co\{P_4Mo_6\}_2$ -based hybrids **2** and **4**, along with excellent recycle stability. This mechanism study shows that the different central metals M in the $M\{P_4Mo_6\}_2$ cluster have a considerable impact on photocatalytic performance due to their regulation effect on the electronic structure. This work provides evidence for the important role of the central metal in hourglass-type phosphomolybdate in the regulation of photocatalytic performance, and it brings inspiration for the design of highly efficient photocatalysts based on polyoxometalates.



KEYWORDS: polyoxometalate, phosphomolybdate, photocatalysis, Cr(VI) reduction

1 Introduction

Rapid industrialization causes an increased release of wastewater containing heavy metal ions, which pose a great threat to human health and environmental safety [1–5]. In particular, hexavalent chromium Cr(VI), which has high carcinogenicity and teratogenicity, is widely found in wastewater from different industrial processes such as metallurgical technology, electroplating,

and medical and chemical engineering. Cr(VI) species have good water solubility and can easily enter the food chain, which increases the threat of severe diarrhea and kidney, bladder, and liver cancers [6–10]. Therefore, the removal of toxic Cr(VI) from environmental water is of crucial importance. At present, reducing toxic Cr(VI) to the less toxic trivalent chromium Cr(III) is one of the most effective treatment methods by means of a variety of techniques, including chemical techniques [11–13], bacterial degradation [14], and biological [15] and photocatalytic technology [16, 17]. Thus, photocatalysis technology with high efficiency, stability, low cost, sustainability, and environmental protection has been considered to be an effective and promising method to tackle Cr(VI) pollution [18, 19]. The key challenge is to develop efficient heterogeneous photocatalytic materials. In photocatalytic reactions, the

Received: December 1, 2022; **Revised:** February 4, 2023

Accepted: February 23, 2023

 Address correspondence to Yuan-Yuan Ma, mayy334@hebtu.edu.cn; Zhan-Gang Han, hanzg116@126.com, hanzg116@hebtu.edu.cn

© The Author(s) 2023. Polyoxometalates published by Tsinghua University Press. The articles published in this open access journal are distributed under the terms of the Creative Commons Attribution 4.0 International License (<http://creativecommons.org/licenses/by/4.0/>), which permits use, distribution and reproduction in any medium, provided the original work is properly cited.



清华大学出版社
Tsinghua University Press

SciOpen

<https://doi.org/10.26599/POM.2023.9140027>

Polyoxometalates, 2023, 2, 9140027

semiconductor photocatalysts absorb photons that are matched with their band gap energy, and they produce electrons (e^-) and holes (h^+) for subsequent photocatalytic redox reactions, which leads to Cr(VI) reduction; the Cr(VI) species in turn can serve as photoelectron scavengers to promote the process of carrier separation and accelerate the efficiency of photocatalytic reactions [20–23]. Recently, various semiconductor photocatalysts have been used in visible light-driven photocatalytic Cr(VI) reduction reactions, including titanium dioxide (TiO_2) [16, 20], cadmium sulfide (CdS) [24], and tungsten trioxide (WO_3) [25, 26]. Some of them suffer from the limited utilization of light, low catalytic efficiency, and poor structural stability, which hinder their practical application. Ideal visible-light photocatalysts should have the following: (i) appropriate band gap for the high utilization of visible light; (ii) low electron (e^-) and hole (h^+) recombination efficiency; (iii) good carrier migration efficiency; (iv) a stable structure for sustainable utilization. Thus, the development of efficient photocatalysts with suitable energy bands, and high photogenerated carrier separation and utilization for the reduction of Cr(VI) to Cr(III) is urgently needed [21, 27].

Polyoxometalates (POMs) are considered to be promising photocatalysts owing to their fascinating molecular nature with uniform active sites, structural diversity, and tunable physicochemical properties [28–34]. In particular, the hourglass-type phosphomolybdate clusters $\{\text{M}^{\text{II}}[\text{P}_4\text{Mo}_6\text{O}_{31}]_2\}^{22-}$ (abbr. $\text{M}\{\text{P}_4\text{Mo}_6\}_2$, $\text{M} = \text{Mn, Co, Fe, etc.}$), as a unique member of the POM family, are constructed of two $[\text{P}_4\text{Mo}_6\text{O}_{31}]^{12-}$ (abbr. $\{\text{P}_4\text{Mo}_6\}$) half-units bridged by one central metal M. It should be pointed out that all Mo centers in the $\text{M}\{\text{P}_4\text{Mo}_6\}_2$ cluster are at a +5 oxidation state and belong to a fully reduced anionic cluster, which endows the $\text{M}\{\text{P}_4\text{Mo}_6\}_2$ cluster with remarkable redox properties that support a rapid, reversible, and stepwise multiple electron transfer process while maintaining the $\text{M}\{\text{P}_4\text{Mo}_6\}_2$ cluster structure [32, 33]. Moreover, $\text{M}\{\text{P}_4\text{Mo}_6\}_2$ clusters could also be regarded as the analogs of semiconductor metal oxides, as they consist of d^1 Mo and oxide ions and display similar electronic attributes, such as a well-defined highest occupied molecular orbital (HOMO) and a well-defined lowest unoccupied molecular orbital (LUMO). Such a feature reveals that the electrons in $\text{M}\{\text{P}_4\text{Mo}_6\}_2$ clusters can be excited from HOMO to LUMO, which is similar to the charge transfer between the valence band (VB) and conduction band (CB) in semiconductors under suitable illumination. Owing to the fascinating optical characteristics, $\text{M}\{\text{P}_4\text{Mo}_6\}_2$ clusters exhibit remarkable photocatalytic application in various reactions [17, 35–38]. Moreover, hourglass-type $\text{M}\{\text{P}_4\text{Mo}_6\}_2$ clusters have strong structural tailoring, and the central metal ions can be adjusted from main group metals to transition metals [22, 39–41]. The well-defined crystalline structures of hourglass-type $\text{M}\{\text{P}_4\text{Mo}_6\}_2$ clusters provide an ideal photocatalyst model for the investigation of the structure–function relationship in photocatalytic Cr(VI) reduction. Therefore, building hourglass-type POM-based materials with wide light absorption abilities and suitable energy band structures is hopeful for achieving the efficient photocatalytic reduction of Cr(VI).

Based on the above considerations, four cases of hourglass-type phosphomolybdate-based crystalline networks— $(\text{H}_2\text{bpe})_2[\text{Mn}(\text{H}_2\text{O})_3]_2\{\text{Mn}[\text{P}_4\text{Mo}_6\text{O}_{31}\text{H}_7]_2\}\cdot 8\text{H}_2\text{O}$ (**1**), $(\text{H}_2\text{bpe})_2[\text{Co}(\text{H}_2\text{O})_3]_2\{\text{Co}[\text{P}_4\text{Mo}_6\text{O}_{31}\text{H}_7]_2\}\cdot 8\text{H}_2\text{O}$ (**2**), $(\text{Hbpe})(\text{H}_2\text{bpe})\text{Na}[\text{Mn}(\text{H}_2\text{O})_3]_2\{\text{Mn}[\text{P}_4\text{Mo}_6\text{O}_{31}\text{H}_7]_2\}\cdot 9\text{H}_2\text{O}$ (**3**), $(\text{Hbpe})(\text{H}_2\text{bpe})\text{Na}[\text{Co}(\text{H}_2\text{O})_3]_2\{\text{Co}[\text{P}_4\text{Mo}_6\text{O}_{31}\text{H}_7]_2\}\cdot 9\text{H}_2\text{O}$ (**4**) (bpe = 1,2-di(4-pyridyl)ethylene) were synthesized

as potential photocatalysts for Cr(VI) reduction. A structural analysis showed that hybrids **1–4** possess similar two-dimensional (2D) inorganic networks, which interact with protonated bpe cations via hydrogen bonding interactions to become three-dimensional (3D) supramolecular structures. When used as photocatalysts, the four hybrids exhibited efficient photocatalytic activity for Cr(VI) reduction, with Cr(VI) removal rates of 91% for hybrid **1**, 74% for hybrid **2**, 90% for hybrid **3**, and 71% for hybrid **4** within 80 min. Such hourglass-type hybrids exhibit high recyclability and structural stability. The reaction mechanism is discussed.

2 Experimental section

2.1 Synthesis of crystals 1–4

(1) $(\text{H}_2\text{bpe})_2[\text{Mn}(\text{H}_2\text{O})_3]_2\{\text{Mn}[\text{P}_4\text{Mo}_6\text{O}_{31}\text{H}_7]_2\}\cdot 8\text{H}_2\text{O}$

A mixture of $(\text{NH}_4)_2\text{Mo}_7\text{O}_{24}\cdot 4\text{H}_2\text{O}$ (0.08 g, 0.07 mmol), $\text{MnCl}_2\cdot 4\text{H}_2\text{O}$ (0.08 g, 0.40 mmol), bpe (0.03 g, 0.16 mmol), H_3PO_4 (0.5 mL, 7.50 mmol), and H_2O (8.0 mL, 0.44 mol) was stirred at room temperature for about 0.5 h. Then, the pH of the solution was adjusted to 2 with 8 M H_3PO_4 and $\text{NH}_3\cdot \text{H}_2\text{O}$. Finally, the solution was placed in a polytetrafluoroethylene-lined autoclave (25 mL) and reacted at 180 °C for 1 day. After the reaction, the solution was slowly cooled to room temperature. Reddish-brown massive crystals were obtained and washed with deionized water. Based on the mass of Mo element, the yield was 65%. The elemental analysis calculated for $\text{C}_{24}\text{H}_{66}\text{Mn}_3\text{Mo}_{12}\text{N}_4\text{O}_{76}\text{P}_8$ (%) was: C, 9.03; H, 2.08; N, 1.76; Mn, 5.13; P, 7.77; Mo, 36.08. Experimental value (%): C, 9.06; H, 1.99; N, 1.79; Mn, 5.16; P, 7.78; Mo, 36.14. The selected IR (solid KBr pellet, cm^{-1}) was: 3410(s), 1623(s), 1507(m), 1425(w), 1374(w), 1345(w), 1286(w), 1216(m), 1122(m), 1077(s), 971(s), 915(m), 823(m), 729(s), 700(m), 607(m).

(2) $(\text{H}_2\text{bpe})_2[\text{Co}(\text{H}_2\text{O})_3]_2\{\text{Co}[\text{P}_4\text{Mo}_6\text{O}_{31}\text{H}_7]_2\}\cdot 8\text{H}_2\text{O}$

The synthetic process of hybrid **2** was similar to that of hybrid **1**, except that $\text{MnCl}_2\cdot 4\text{H}_2\text{O}$ was replaced by $\text{Co}(\text{NO}_3)_2\cdot 6\text{H}_2\text{O}$ (0.08 g, 0.27 mmol), and the pH of the solution was adjusted to 2.5 with 8 M H_3PO_4 and $\text{NH}_3\cdot \text{H}_2\text{O}$. Reddish-brown massive crystals were obtained. The yield based on the mass of Mo element was 42%. The elemental analysis calculated for $\text{C}_{24}\text{H}_{66}\text{Co}_3\text{Mo}_{12}\text{N}_4\text{O}_{76}\text{P}_8$ (%) was: C, 9.00; H, 2.08; N, 1.75; Co, 5.52; P, 7.74; Mo, 37.97. Experimental value (%): C, 9.04; H, 1.98; N, 1.80; Co, 5.56; P, 7.68; Mo, 38.01. The selected IR (solid KBr pellet, cm^{-1}) was: 3411(s), 1633(s), 1511(m), 1386(s), 1347(w), 1289(w), 1219(w), 1120(w), 1071(m), 1020(s), 961(s), 920(m), 818(w), 744(m), 695(w), 611(w).

(3) $(\text{Hbpe})(\text{H}_2\text{bpe})\text{Na}[\text{Mn}(\text{H}_2\text{O})_3]_2\{\text{Mn}[\text{P}_4\text{Mo}_6\text{O}_{31}\text{H}_7]_2\}\cdot 9\text{H}_2\text{O}$

The synthetic process of hybrid **3** was similar to that of hybrid **1**, except that the pH of the solution was adjusted to 2 with 8 M H_3PO_4 and 4 M NaOH. After the reaction, reddish-brown strip crystals were obtained. Based on the mass of Mo element, the yield of hybrid **3** was calculated as 44%. The elemental analysis calculated for $\text{C}_{24}\text{H}_{73}\text{NaMn}_3\text{Mo}_{12}\text{N}_4\text{O}_{80}\text{P}_8$ (%) was: C, 8.78; H, 2.24; N, 1.71; Na, 0.70; Mn, 5.18; P, 7.54; Mo, 35.05. Experimental value (%): C, 8.83; H, 2.20; N, 1.69; Na, 0.73; Mn, 5.13; P, 7.61; Mo, 35.02. The selected IR (solid KBr pellet, cm^{-1}) was: 3414(s), 1631(s), 1507(m), 1382(s), 1207(w), 1059(s), 1028(s), 960(s), 828(w), 737(m), 698(w), 602(w).

(4) (Hbpe)(H₂bpe)Na[Co(H₂O)₃]₂[Co{P₄Mo₆O₃₁H₇}]₂·9H₂O

The synthesis process of hybrid **4** was similar to that of hybrid **2**, except that the pH condition of the reaction solution was 2.0. After the reaction, the reddish-brown massive crystals were obtained. Based on the mass of Mo element, the yield of hybrid **4** was calculated to be 58%. The elemental analysis calculated for C₂₄H₇₃NaCo₃Mo₁₂N₄O₈₀P₈ (%) was: C, 8.74; H, 2.23; N, 1.70; Na, 0.70; Co, 5.36; P, 7.52; Mo, 34.92. Experimental value (%): C, 8.70; H, 2.26; N, 1.73; Na, 0.69; Co, 5.33; P, 7.57; Mo, 34.95. The selected IR (solid KBr pellet, cm⁻¹) was: 3410(s), 1629(s), 1511(m), 1381(s), 1346(w), 1289(w), 1208(w), 1121(m), 1061(s), 967(s), 913(m), 818(w), 731(s), 687(m), 611(m).

2.2 Photocatalytic experiments

The photocatalytic reactions were carried out in a WP-TEC-1020 photocatalytic parallel reactor, which simulates natural light. At room temperature, the light source was 10 W white light with low energy consumption. The reaction process was as follows: 20 mg crystals as a heterogeneous photocatalyst, sacrificial agent isopropanol (IPA) (7.5 mL), and K₂Cr₂O₇ (7.5 mL, 3.8 × 10⁻⁴ M) were mixed in the reactor and stirred under dark conditions for 30 min to enable the solid hybrids **1–4** to reach adsorption/desorption equilibrium, and then the reactor was set under an illumination of 10 W white light. Next, 1.00 mL of reaction solution was taken from the reaction system every 10 min and measured using ultraviolet visible (UV-vis) spectrophotometry. Each data point was determined by the calculated average values from three parallel experiments.

According to the Lambert-Beer law, when the conditions of incident light, absorption coefficient, and path length are consistent, the absorbance of a solution increases with an increase in solution concentration. Therefore, within a certain range, the concentration *c* and absorbance (*A*) comply with Lambert's Law, $A = kbc$, where *A* is the absorbance, *k* is the molar absorption coefficient, *b* is the liquid layer thickness, and *c* is the solution concentration. Therefore, its conversion can also be expressed as $D = (A_0 - A_t)/A_0 \times 100\%$, where *D* is the conversion rate, *A*₀ is the initial solution absorbance, and *A*_{*t*} is the solution absorbance with respect to the reaction time. Thus, according to $([c_0] - [c_t])/c_0 \times 100\%$, [*c*₀] is the initial solution concentration, and [*c*_{*t*}] is the concentration of the solution at *t* min; the Cr(VI) reduction rate can be obtained via the absorbance intensity at 353 nm of the UV spectrum.

2.3 Active species trapping experiments

In order to explore the reaction mechanism of hybrids **1–4** in the photocatalytic Cr(VI)-IPA system, 1 mM AgNO₃ and EDTA-2Na were used as the electron (e⁻) scavenger and hole (h⁺) scavenger, respectively, to detect the active species in the photocatalytic reduction of Cr(VI).

3 Results and discussion

3.1 Synthesis and structural characterization

The four hourglass-type phosphomolybdate-based crystalline hybrids **1–4** were synthesized using a one-step hydrothermal reaction of transition metal salts (M = Co²⁺, Mn²⁺), (NH₄)₂Mo₇O₂₄·4H₂O, H₃PO₄, and bpe. During the hydrothermal synthesis process, the reaction conditions, which include the reaction pH values and regulators, play important roles in the

formation of the final product. Hybrids **1** and **3** were prepared under the same reaction temperature and pH conditions, except that NH₃·H₂O was introduced to adjust the pH condition of hybrid **1**. If NaOH was used to adjust the pH, hybrid **3** was obtained. The reaction pH conditions affected the formation of hybrids **2** and **4**. Hybrid **2** was synthesized at pH = 2.5, and hybrid **4** was synthesized at a pH of 2.0. The bond valence sum calculation shows that all P and Mo atoms in hybrids **1–4** are +5 oxidation states, and Mn and Co ions are +2 oxidation states (Table S1 in the Electronic Supplementary Material (ESM)).

A single-crystal X-ray diffraction (XRD) analysis showed that hybrids **1–4** belong to the triclinic crystal system *P*₁ space group. Among the hybrids, hybrids **1** and **2** possess an isomorphous structure, and the structures of hybrids **3** and **4** are also isomorphous (Tables S2–S11 in the ESM). Taking hybrids **1** and **3** as examples, the crystallographic asymmetric unit of hybrid **1** consists of one {Mn{P₄Mo₆O₃₁H₇}}⁸⁻ (abbr. Mn{P₄Mo₆}) polyoxoanion cluster, two protonated [H₂bpe]²⁺, two hydrated metal ions [Mn(H₂O)₃]²⁺, and eight lattice water molecules. There are two types of crystallographically independent Mn centers (Mn1 and Mn2). Mn1, as the central metal ion of the Mn{P₄Mo₆}} cluster has a hexacoordinated octahedral configuration to bridge the two [P₄Mo₆O₃₁]¹²⁻ subunits together, via six shared μ₃-O atoms, to become an hourglass-type Mn{P₄Mo₆}} cluster, in which the Mn1–O bond lengths are 2.153–2.231 Å. The Mn2 center also presents a hexacoordinated environment to coordinate with three oxygen atoms from three {PO₄} units of three Mn{P₄Mo₆}} clusters, and three coordination water molecules at Mn2–O distances of 2.055(5)–2.228(5) Å. In hybrid **1**, the Mn2 centers links the three adjacent Mn{P₄Mo₆}} clusters together to form an inorganic 2D sheet-like structure. It should be pointed out that there are six Mn2 centers surrounding one Mn{P₄Mo₆}} cluster, and they are oriented in the direction of six {PO₄} units on the outer-edge of Mn{P₄Mo₆}} (Fig. S1(a) in the ESM). In hybrid **1**, the Mn2 centers can be viewed as three-connection nodes and the Mn{P₄Mo₆}} clusters can be viewed as six-connection nodes; thus the 2D layers possess a 3,6-connected *kgd*; Shubnikov plane (3.6.3.6)/dual net with a point symbol of {4²}_2{4⁶.6⁸} (Figs. 1(a) and 1(b)). These 2D inorganic layers are arranged in parallel on the *ab* plane. The protonated organic bpe cations fill the space between the layers and interact with these 2D inorganic Mn{P₄Mo₆}} clusters via abundant hydrogen bonding interactions to create a 3D supramolecular network (Figs. 1(c) and 1(d)).

Hybrid **3** has a structural unit similar to that of hybrid **1**. The crystallographic asymmetric unit of hybrid **3** contains one Mn{P₄Mo₆}} polyoxoanion cluster, one bi-protonated [H₂bpe]²⁺, one monoprotinated [Hbpe]⁺, two hydrated [Mn(H₂O)₃]²⁺ ions, one Na⁺ ion, and nine lattice water molecules. Notably, there are four kinds of crystallographically independent Mn centers (Mn1, Mn2, Mn3, and Mn4) in hybrid **3** (Figs. S1(b) in the ESM and Figs. 2(a) and 2(b)). Among the Mn centers, Mn1 and Mn2 exhibit typical six-coordination modes as central metals to connect two {P₄Mo₆}} half-units together to form hourglass Mn{P₄Mo₆}} clusters with Mn1–O bond lengths of 2.151–2.227 Å, and Mn2–O bond lengths of 2.148–2.228 Å. Mn3 and Mn4 also adopt a hexacoordinated octahedral configuration that is defined by four oxygen atoms from three Mn{P₄Mo₆}} clusters and two coordination water molecules, with Mn–O distances of 2.048–2.301 Å. The dissociative Na⁺ ion is located at the center of the Mn3 and Mn4 centers. Both the Mn3 and Mn4 centers serve as three-

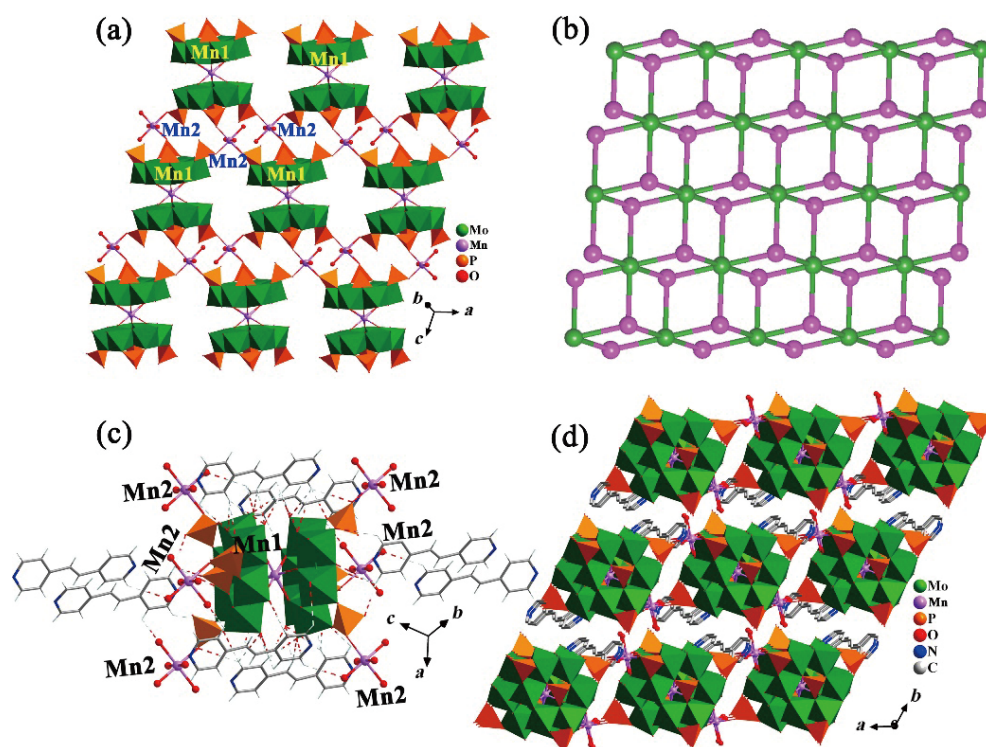


Figure 1 (a) 2D inorganic sheet of hybrid 1. (b) 2D inorganic simplified diagram of hybrid 1 (the green balls represent $\text{Mn}\{\text{P}_4\text{Mo}_6\}_2$ clusters and the pink balls represent the bridging unit $([\text{Mn}(\text{H}_2\text{O})_3]^{2+})$). (c) The “core-shell” structure of the inorganic and organic components of hybrid 1 and the coordination environment of Mn^{2+} . (d) 3D supramolecular stacking structure of hybrid 1.

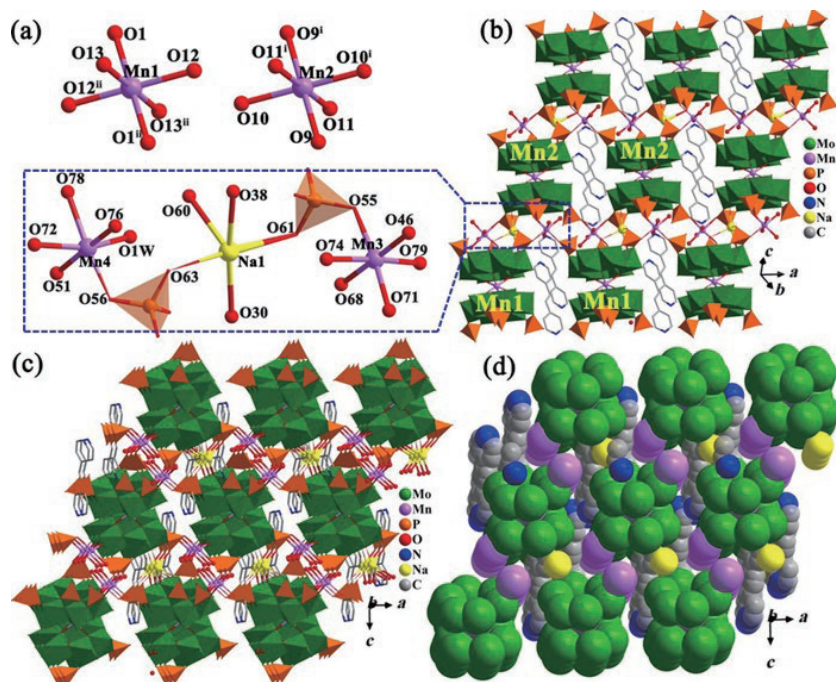


Figure 2 (a) Coordination environments of Mn1–Mn4 and Na1 ($i = -x, 2-y, -z$; $ii = 1-x, 1-y, 1-z$). (b) Packing mode of 2D inorganic anions and organic cations in hybrid 3. (c) and (d) 3D supramolecular structure of hybrid 3.

connection nodes that link the surrounding three $\text{Mn}\{\text{P}_4\text{Mo}_6\}_2$ clusters together to expand the structure into 2D inorganic layers. These 2D layers in hybrid 3 present a similar 3,6-connected *kgd*; Shubnikov plane (3.6.3.6)/dual net to hybrid 1 with a point symbol of $\{4^3\}_2\{4^6.6^3.8^3\}$ (Fig. 2(b)). The protonated organic bpe cations are located on the upper and lower sides of the interstices in the 2D

layers and interacted with 2D layers with abundant hydrogen bonding interactions, forming a 3D supramolecular structure (Figs. 2(c) and 2(d)). Considering their similar structural fragments, hybrids 1–4 provide a distinct structural model of photocatalysts in an investigation of the structure–function relationship in photocatalytic Cr(VI) reduction.

3.2 Physical characterizations

The compositions and structures of hybrids **1–4** were further characterized by Fourier transform infrared (FT-IR) spectroscopy, powder XRD and thermogravimetric (TG) analysis. Figure S2 in the ESM shows the IR spectra of hybrids **1–4**, in which the characteristic absorption peaks at 600–750, 815–975, and 1020–1220 cm^{-1} are attributed to the contraction vibration of $\nu(\text{Mo}-\text{O}-\text{Mo})$, $\nu(\text{Mo}=\text{O})$, and $\nu(\text{P}-\text{O})$ of the hourglass-type $\text{M}\{\text{P}_4\text{Mo}_6\}_2$ clusters. The absorption peaks in the range of 1380–1635 cm^{-1} are assigned to the stretching vibrations of the C=C and C=N bonds of the bpe cations. The XRD patterns of hybrids **1–4** in Fig. S3 in the ESM demonstrate a good match between the experimental and the simulated data, which indicates good phase purities of hybrids **1–4**. In addition, the TG curves of hybrids **1–4** show two weight loss steps that correspond to the loss of water molecules and organic species. All four hybrids maintain their structures at approximately 200 °C, which implies their good thermal stabilities (Fig. S4 in the ESM).

Furthermore, the redox properties of hybrids **1–4** were studied using the cyclic voltammetry technique with a three-electrode system. As shown in Fig. S5 in the ESM, hybrids **1–4** exhibit three pairs of quasi-reversible redox peaks (I–I', II–II', III–III') in the range of -0.1 – 0.8 V vs. Ag/AgCl. The three pairs of redox peaks are assigned to the two-, four-, and six-electron gain-and-loss process of hourglass-type $\{\text{M}(\text{P}_4\text{Mo}_6)_2\}$ clusters. Moreover, the peak currents of three pairs of redox peaks also show a linear correlation with the square root of the scanning speeds (Fig. S5 in the ESM). This result indicates that hybrids **1–4** have stable electrochemical redox characteristics and they are potential catalytic materials for Cr(VI) degradation.

To explore the optical properties of hybrids **1–4**, the solid-state UV–vis diffuse reflectance absorption (DRS) spectrum was conducted. As shown in Fig. 3(a), hybrids **1–4** display strong and wide absorption bands in the range of 200–800 nm, which is a prerequisite for exploring the application of these reduced molybdenum phosphate photocatalysts. According to the Kubelka–Munk formula, the band gaps (E_g) of hybrids **1–4** were calculated as 2.48, 2.61, 2.53, and 2.57 eV (Fig. 3(b)), which revealed their typical semiconductor features ($1 \text{ eV} < E_g < 3 \text{ eV}$). Moreover, the energy band structures of hybrids **1–4**, including the positions of conduction band (CB) and valence band (VB) were determined using the Mott–Schottky technique. As shown in Figs. 3(c)–3(f), hybrids **1–4** demonstrate typical n-type semiconductor behaviors due to their positive slopes at 2000, 2500, and 3000 Hz, from which the CB potentials of hybrids **1–4** were calculated to be -0.34 V vs. Ag/AgCl for **1**, -0.34 V vs. Ag/AgCl for **2**, -0.38 V vs. Ag/AgCl for **3**, and -0.43 V vs. Ag/AgCl for **4**, respectively. Relative to the standard hydrogen electrode (vs. NHE), the CB potentials of hybrids **1–4** converted to -0.14 , -0.14 , -0.18 , and -0.23 eV, respectively. When these results were combined with the results of the UV–vis DRS spectra, the VB positions of hybrids **1–4** were obtained, which were 2.34, 2.47, 2.35, and 2.34 eV vs. NHE, respectively. It was found that the CB potentials of hybrids **1–4** were much more negative than that of Cr(VI)/Cr(III) (0.51 V, pH = 6.8), which suggests thermodynamic feasibility for the photocatalytic reduction of Cr(VI). In addition, comparing the energy band positions of hybrids **1–4** (Fig. 3(g)), it can be observed that hybrids **1** and **3** have a narrower band gap than hybrids **2** and **4**, which is conducive to photogenerated electron transfer process and producing a strong capability for the photocatalytic reduction

of Cr(VI).

3.3 Photocatalytic Cr(VI) reduction properties

The photocatalytic Cr(VI) reduction properties of hybrids **1–4** were evaluated using a $\text{K}_2\text{Cr}_2\text{O}_7$ -IPA redox system under irradiation by 10 W white light. As shown in Fig. 4(a), the photocatalytic Cr(VI) reduction reaction over hybrids **1–4** proceeded rapidly, and the conversion rate of Cr(VI) within 80 min reached 91% for **1**, 74% for **2**, 90% for **3**, and 71% for **4**, respectively (Figs. 4(a) and 4(b)). These results demonstrate the excellent photocatalytic performance of hybrids **1–4**, which is better than that of most reported materials (Table 1). To understand the activity origin of hybrids **1–4**, a series of control experiments were carried out. As shown in Fig. 4(a), when the reaction was performed under no light or no catalyst, the Cr(VI) species were reduced very little, which suggests the good photocatalytic activity of hybrids **1–4**. Given that there were protonated bpe cations in the structures of hybrids **1–4**, bpe was selected as a control photocatalyst, and it showed no activity in the conversion of Cr(VI), thus eliminating any effect of bpe on the photocatalytic reaction. Considering that the main structures (2D inorganic layer) of hybrids **1–4** are composed of metal–oxygen bonds, they can be viewed as the aggregation of metal oxides at the nanoscale. Thus, Na_2MoO_4 , MnO, and CoO were selected as control samples. As stated in our previous report, Na_2MoO_4 exhibited a Cr(VI) conversion rate of approximately 14% [42]. Furthermore, very little photocatalytic Cr(VI) reduction over MnO and CoO occurred. These results show the structure advantages of hourglass-type $\text{M}\{\text{P}_4\text{Mo}_6\}_2$ clusters and reveal that the hourglass-type $\text{M}\{\text{P}_4\text{Mo}_6\}_2$ cluster is the active component in the photocatalytic Cr(VI) reduction reaction. The photocatalytic performances of hybrids **1** and **3** (91% and 90%) are obviously better than those of hybrids **2** and **4** (74% and 71%). Considering their similar 2D inorganic layer and organic cation bpe, the difference in photocatalytic activities may originate from the hourglass-type $\text{M}\{\text{P}_4\text{Mo}_6\}_2$ clusters having different central metal ions (Mn centers for **1** and **3**, Co centers for **2** and **4**). Our previous work found that the transition metal-centered $\text{M}\{\text{P}_4\text{Mo}_6\}_2$ clusters showed better photocatalytic activity than did the main group metal-centered $\text{M}\{\text{P}_4\text{Mo}_6\}_2$ clusters [22]. This experimental result suggested that on the premise of an isomorphous structure, Mn $\{\text{P}_4\text{Mo}_6\}_2$ -based hybrids display better photocatalytic performance than do Co $\{\text{P}_4\text{Mo}_6\}_2$ -based hybrids. As for hybrids **1** and **3**, both compounds were constructed of $\{\text{Mn}(\text{P}_4\text{Mo}_6)_2\}$ clusters and bridged Mn centers. The slight difference in their activities may be attributed to the difference in connection mode between the Mn $\{\text{P}_4\text{Mo}_6\}_2$ clusters and the bridged Mn centers, which has only a slight influence on photocatalytic activity for Cr(VI) reduction. To gain further insight into their photocatalytic activity, the reaction kinetics of photocatalytic Cr(VI) reduction was investigated. As shown in Fig. 4(c), the reaction follows pseudo first-order kinetics with Cr(VI) concentration, and the reaction rate constants k derived from the slope of the kinetics curves are 0.0237 min^{-1} for **1**, 0.0143 min^{-1} for **2**, 0.0221 min^{-1} for **3**, and 0.0134 min^{-1} for **4**. This result indicates that Mn $\{\text{P}_4\text{Mo}_6\}_2$ -based hybrids have faster photocatalytic reaction kinetics than do Co $\{\text{P}_4\text{Mo}_6\}_2$ -based hybrids. When these results are combined with the energy bands of hybrids **1–4**, it can be observed that Mn $\{\text{P}_4\text{Mo}_6\}_2$ -based hybrids **1** and **3** have a narrower band gap for photocatalytic Cr(VI) reduction than do the Co $\{\text{P}_4\text{Mo}_6\}_2$ -based hybrids **2** and **4**. This observation reveals that the regulation of central metals in hourglass-type $\text{M}\{\text{P}_4\text{Mo}_6\}_2$

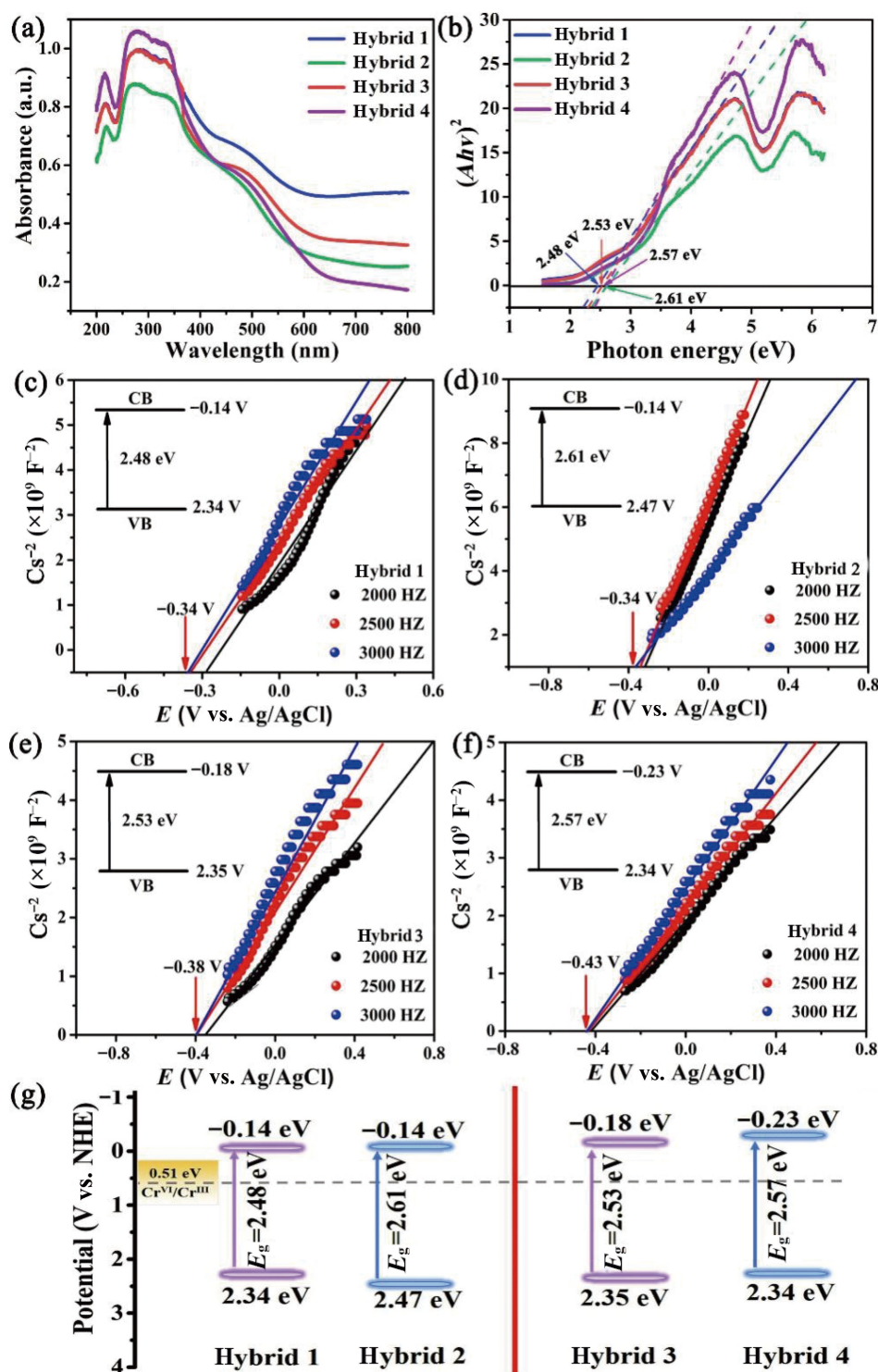


Figure 3 (a) UV-vis DRS spectra of hybrids 1–4. (b) Band gap energies of hybrids 1–4 according to the Kubelka–Munk formula. (c)–(f) Mott–Schottky plots of hybrids 1 (c), 2 (d), 3 (e), and 4 (f). (g) Band positions of hybrids 1–4.

clusters can modulate their electron structure, thus promoting their photocatalytic performance.

Moreover, to further understand the photocatalytic activities of hybrids 1–4, photocurrent response experiments were conducted to investigate the separation efficiency of the photogenerated electron–hole pairs. As shown in Fig. 4(d), pure indium-tin oxide (ITO) glass has no response to visible light. In contrast, hybrids 1–4

generate relatively high photo-current intensities under the condition of continuously turning light on and off. In particular, the photocurrent intensities of hybrids 1 and 3 are remarkably higher than those of hybrids 2 and 4, indicating that hybrids 1 and 3 have higher separation efficiency of the photogenerated carriers. Furthermore, the fluorescence emission spectrum test (Fig. 4(e)) found that hybrids 1 and 3 showed lower fluorescence intensity

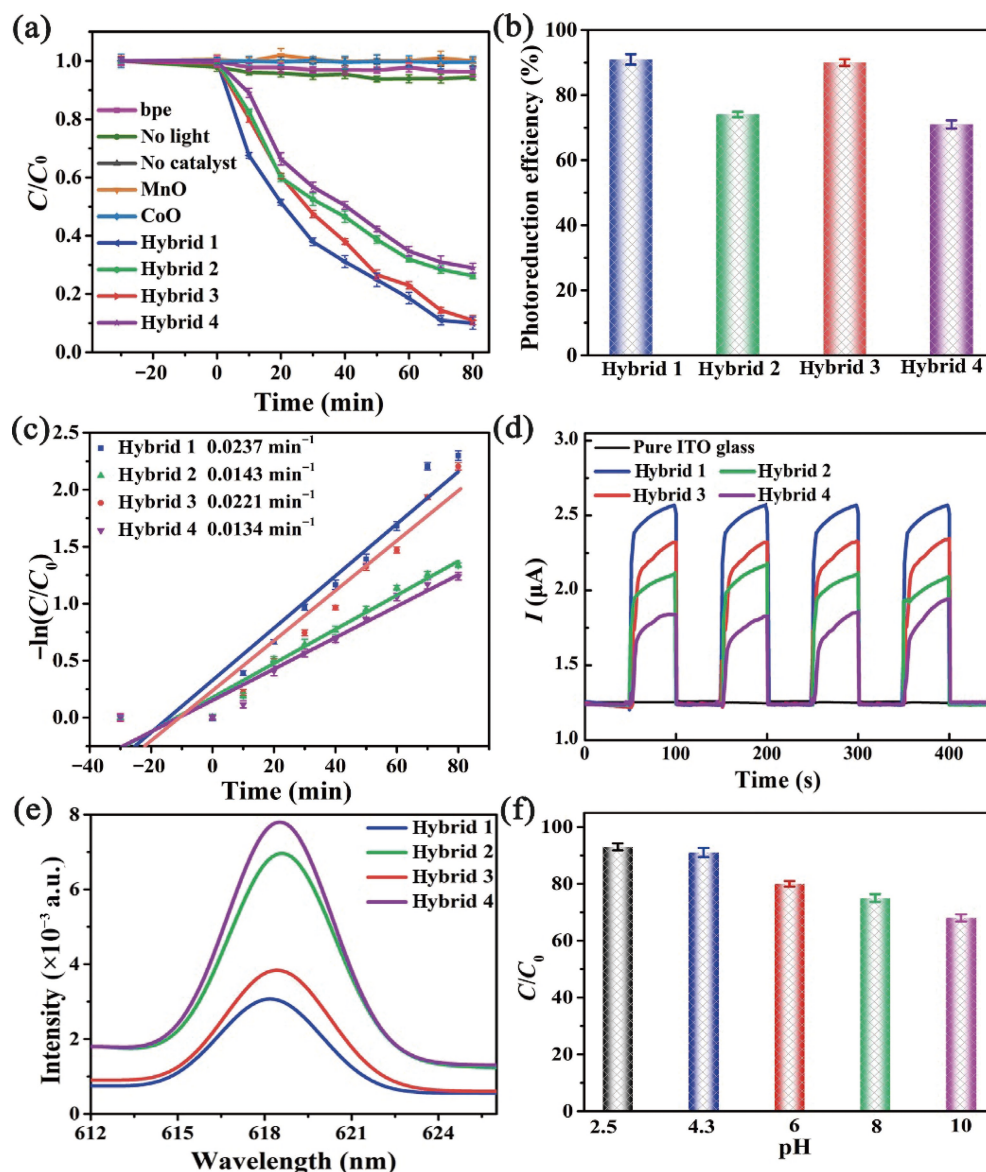


Figure 4 (a) Profiles of photocatalytic Cr(VI) reduction in the presence of 1–4. (b) Performance histograms of photocatalytic Cr(VI) reduction over hybrids 1–4. (c) First-order kinetics diagrams of 1–4 for the photocatalytic reduction of Cr(VI). (d) Transient photocurrent responses of 1–4. (e) Fluorescence emission spectrum of 1–4. (f) Histogram comparisons of Cr(VI) photocatalytic reduction efficiency at different pH levels.

than hybrids 2 and 4, indicating that $Mn\{P_4Mo_6\}_2$ -based hybrids can inhibit the recombination of photogenerated carriers, thus significantly accelerating the photocatalytic Cr(VI) reduction reaction.

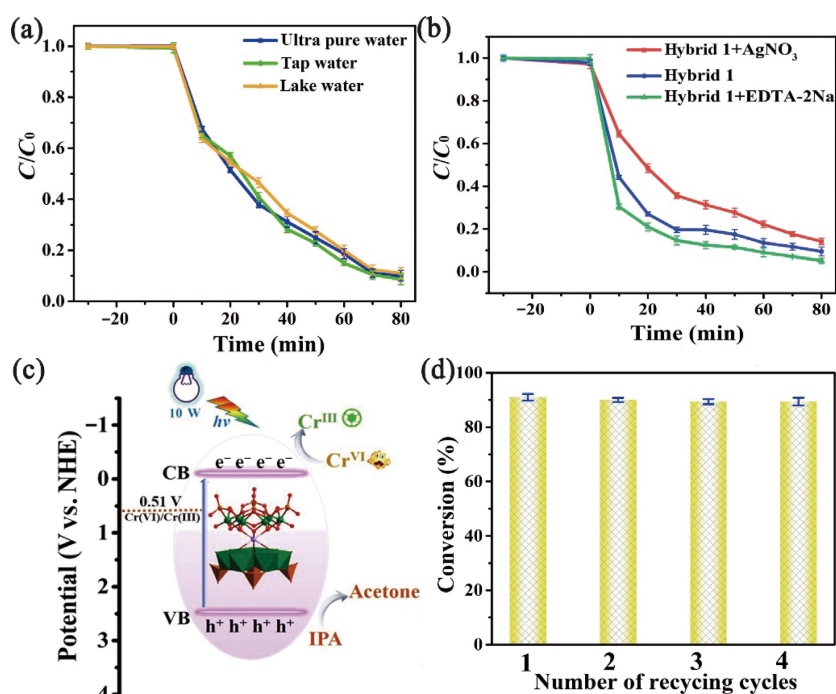
To evaluate the practical application of these hybrids, hybrid 1 was selected as a representative for use in a photocatalytic Cr(VI) reduction reaction under different pH conditions (pH = 2.5, 4.3 (initial pH of $K_2Cr_2O_7$ solution), 6.0, 8.0, and 10.0) and in real water samples. As shown in Fig. 4(f), hybrid 1 shows high Cr(VI) degradation efficiencies at various pH levels from 2.5–10. The conversion rates of Cr(VI) are 93% at a pH of 2.5, 91% at a pH of 4.3, 80% at a pH of 6.0, 75% at a pH of 8.0, and 68% at a pH of 10.0. It can be observed that the photocatalytic performance of hybrid 1 gradually decreases with an increase in pH values. The acidic environment is more conducive to the photocatalytic reduction of Cr(VI); this may be caused by the different Cr(VI) reduction mechanisms under different pH conditions. Moreover, tap water

and lake water were used as the solvents in the Cr(VI) solution to assess the practical application of hybrid 1. As shown in Fig. 5(a), the reduction efficiencies of Cr(VI) in tap water and lake water are 91% and 89%, respectively. This result is consistent with the photocatalytic performance in a pure water system, which indicates that hybrid 1 shows good photocatalytic performance in reducing Cr(VI) in real water samples and demonstrates its important practical potential.

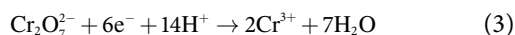
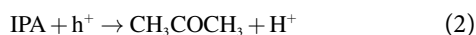
Additionally, the photocatalytic Cr(VI) removal mechanism was evaluated by adding a series of scavengers ($AgNO_3$ and ethylenediaminetetraacetic acid disodium salt (EDTA-2Na)) in the photocatalytic system. Taking hybrid 1 as an example, $AgNO_3$ was used as the electron (e^-) scavenger, and EDTA-2Na was chosen as the hole (h^+) scavenger. As shown in Fig. 5(b), with the addition of EDTA-2Na, the photocatalytic Cr(VI) reduction efficiency over hybrid 1 was improved, whereas the addition of $AgNO_3$ reduced the catalytic efficiency from 91% to 85%. This result indicates that e^-

Table 1 Comparison of the catalytic activities of hybrids 1–4 with those of reported materials for the photocatalytic reduction of Cr(VI)

Photocatalysts	Light source	Dose (mg)	V (mL)	C (mg/L)	Time (min)	R (%)	Ref.
Carbon/SnS ₂ /MCS	300 W Xe lamp	50	100	50	120	63.2	[43]
PMo ₁₂ /TiO ₂ /Ag-X	300 W Xe lamp	20	40	10-50	60	71.1	[44]
CuS@MIL-125	500 W Xe lamp	25	50	48	70	52	[47]
CdS/P ₂ Mo _x W _{18-x}	500 W Xe lamp	30	30	40	100	64	[48]
Bi ₄ Ti ₃ O ₁₂ /Bi ₂ Ti ₂ O ₇	300 W Xe lamp	150	100	1.5	120	90	[45]
{Co[P ₄ Mo ₆ O ₃₁] ₂ }	10 W LED	20	15	112	120	82	[46]
Hybrid 1	10 W LED	20	15	112	80	91	This work
Hybrid 2	10 W LED	20	15	112	80	74	This work
Hybrid 3	10 W LED	20	15	112	80	90	This work
Hybrid 4	10 W LED	20	15	112	80	71	This work

**Figure 5** (a) Profiles of the photoreduction of Cr(VI) in different water samples under visible-light irradiation. (b) Catalytic efficiency of Cr(VI) in the presence of scavengers. (c) Possible photocatalytic reaction mechanism of these hybrids for Cr(VI) reduction under 10 W visible-light irradiation. (d) Recycling experiments for the photo-reduction of Cr(VI).

is the main active species in the photocatalytic Cr(VI) reduction reaction. On this basis, a possible mechanism for photocatalytic Cr(VI) reduction is proposed. Under visible light irradiation, the Mn{P₄Mo₆}₂-based hybrid 1 could be excited to produce photogenerated electrons and holes; e^- immediately participates in the reduction of Cr(VI); and h^+ participates in the oxidation of IPA, which accelerates the separation efficiency of the photogenerated carriers and promotes photocatalytic performance (Fig. 5(c)).



In addition, the stability, and recyclability of photocatalysts are also important factors in practical applications. As shown in Fig. 5(d), hybrid 1 as a photocatalyst drives the photocatalytic

Cr(VI) reduction reaction smoothly for four cycles, and the reduction rates of Cr(VI) remain above 89%. The slight decrease in the photocatalytic efficiency may be caused by the loss of a small amount of photocatalyst during the recovery process. The IR and XRD spectra of hybrid 1 before and after the catalytic reaction show that hybrid 1 maintains good structural integrity (Figs. 6(a) and 6(b)). Moreover, energy-dispersive spectroscopy and X-ray photoelectron spectroscopy (XPS) were employed to characterize the composition and valence state of hybrid 1 after the recycling experiments. Table S12 in the ESM shows that the ratio of P:Mo elements is approximately 2:3, in accordance with the crystal structure of hybrid 1. The XPS full spectrum also shows the presence of P, Mo, Mn, C, N, and O elements in hybrid 1 (Fig. 6(c)). The high resolution Mo XPS spectrum in Fig. 6(d) presents two peaks at 231.69 and 234.85 eV, which can be assigned to the Mo⁵⁺ 3d_{5/2} and Mo⁵⁺ 3d_{3/2} signals, indicating that the valence

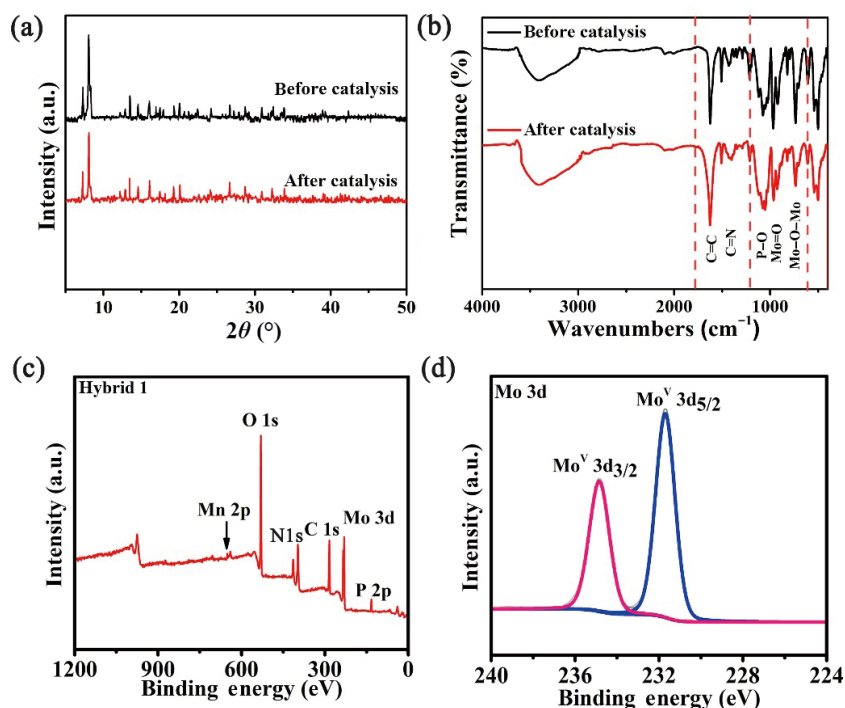


Figure 6 (a) XRD patterns of hybrid 1 before and after photocatalytic experiments. (b) Infrared spectra of hybrid 1 before and after photocatalytic experiments. (c) Overall XPS spectrum of hybrid 1 after the recycling experiment. (d) High-resolution XPS spectrum of Mo in hybrid 1 after the recycling experiment.

of the Mo element does not change after the photocatalytic reaction. These results show that hybrid 1 has good photocatalytic durability and structural stability during the process of photoreduction of Cr(VI).

4 Conclusion

In conclusion, four photoactive hourglass-type phosphomolybdate-based crystalline networks were synthesized for photocatalytic Cr(VI) reduction. Hybrids 1–4 show a similar 2D inorganic layer, with 3,6-connected *kgd* topology constructed from $M\{P_4Mo_6\}_2$ clusters having different central metal ions, wide visible-light absorption, and a suitable energy band structure. The four hybrids showed good photocatalytic performance for Cr(VI) reduction under the irradiation of 10 W white light. The $Mn\{P_4Mo_6\}_2$ -based hybrids 1 and 3 showed Cr(VI) reduction rates of 91% and 90% Cr(VI) within 80 min, which is superior to that of the $Co\{P_4Mo_6\}_2$ -based hybrids 2 and 4 (74% and 71%). Moreover, these hybrids showed good structural stability and recyclability. This work provides a new approach to the design and preparation of green, efficient, and stable photocatalysts for the reduction of Cr(VI).

Electronic Supplementary Material: Supplementary material (including experimental section, IR spectra, XRD patterns, TG curves, CV curves and UV absorption spectra, tables of BVS calculation data, crystallographic data, bond lengths and angles and EDS data) is available in the online version of this article at <https://doi.org/10.26599/POM.2023.9140027>.

Acknowledgements

This research was financially supported by the National Natural Science Foundation of China (Nos. 21871076 and 21901060), the Natural Science Foundation of Hebei Province (Nos. B2020205008,

B2022205005, B2019205074, and B2016205051), the Science and Technology Project of Hebei Education Department (No. BJ2020037), the China Postdoctoral Science Foundation funded Project (No. 2021TQ0095), the Science Foundation of Hebei Normal University (No. L2019B15), the Innovation Capability Improvement Plan Project of Hebei Province (No. 22567604H), and College Student Science and Technology Innovation Project of Hebei Province (No. 202210094002).

Declaration of competing interest

The authors have no competing interests to declare that are relevant to the content of this article.

Author contribution statement

The manuscript was written through contributions of all authors.

References

- [1] Bansod, B.; Kumar, T.; Thakur, R.; Rana, S.; Singh, I. A review on various electrochemical techniques for heavy metal ions detection with different sensing platforms. *Biosens. Bioelectron.* **2017**, *94*, 443–455.
- [2] Saidur, M. R.; Aziz, A. R. A.; Basirun, W. J. Recent advances in DNA-based electrochemical biosensors for heavy metal ion detection: A review. *Biosens. Bioelectron.* **2017**, *90*, 125–139.
- [3] Wang, X. X.; Qi, Y. X.; Shen, Y.; Yuan, Y.; Zhang, L. D.; Zhang, C. Y.; Sun, Y. H. A ratiometric electrochemical sensor for simultaneous detection of multiple heavy metal ions based on ferrocene-functionalized metal-organic framework. *Sens. Actuators B: Chem.* **2020**, *310*, 127756.
- [4] Bashir, M. S.; Ramzan, N.; Najam, T.; Abbas, G.; Gu, X. L.; Arif, M.; Qasim, M.; Bashir, H.; Shah, S. S. A.; Sillanpää, M. Metallic nanoparticles for catalytic reduction of toxic hexavalent chromium

- from aqueous medium: A state-of-the-art review. *Sci. Total Environ.* **2022**, *829*, 154475.
- [5] Jin, M. T.; Yuan, H.; Liu, B.; Peng, J. J.; Xu, L. P.; Yang, D. Z. Review of the distribution and detection methods of heavy metals in the environment. *Anal. Methods* **2020**, *12*, 5747–5766.
- [6] Fu, Y.; Wang, L. L.; Peng, W. Y.; Fan, Q. Y.; Li, Q. C.; Dong, Y. X.; Liu, Y. J.; Boczkaj, G.; Wang, Z. H. Enabling simultaneous redox transformation of toxic chromium(VI) and arsenic(III) in aqueous media—A review. *J. Hazard. Mater.* **2021**, *417*, 126041.
- [7] Lai, Y. J.; Tseng, W. L. Role of 5-thio-(2-nitrobenzoic acid)-capped gold nanoparticles in the sensing of chromium(VI): Remover and sensor. *Analyst* **2011**, *136*, 2712–2717.
- [8] Qian, J.; Zhou, J. M.; Wang, L. L.; Wei, L.; Li, Q.; Wang, D. B.; Wang, Q. L. Direct Cr (VI) bio-reduction with organics as electron donor by anaerobic sludge. *Chem. Eng. J.* **2017**, *309*, 330–338.
- [9] Stern, C. M.; Jegede, T. O.; Hulse, V. A.; Elgrishi, N. Electrochemical reduction of Cr(VI) in water: Lessons learned from fundamental studies and applications. *Chem. Soc. Rev.* **2021**, *50*, 1642–1667.
- [10] Ye, Z. X.; Yin, X. B.; Chen, L. F.; He, X. Y.; Lin, Z. M.; Liu, C. C.; Ning, S. Y.; Wang, X. P.; Wei, Y. Z. An integrated process for removal and recovery of Cr(VI) from electroplating wastewater by ion exchange and reduction-precipitation based on a silica-supported pyridine resin. *J. Clean. Prod.* **2019**, *236*, 117631.
- [11] Gong, K. N.; Wang, W. J.; Yan, J. S.; Han, Z. G. Highly reduced molybdophosphate as a noble-metal-free catalyst for the reduction of chromium using formic acid as a reducing agent. *J. Mater. Chem. A* **2015**, *3*, 6019–6027.
- [12] Xin, X.; Tian, X. R.; Yu, H. T.; Han, Z. G. Synthesis of hybrid phosphomolybdates and application as highly stable and effective catalyst for the reduction of Cr(VI). *Inorg. Chem.* **2018**, *57*, 11474–11481.
- [13] Wang, C. C.; Du, X. D.; Li, J.; Guo, X. X.; Wang, P.; Zhang, J. Photocatalytic Cr(VI) reduction in metal-organic frameworks: A mini-review. *Appl. Catal. B: Environ.* **2016**, *193*, 198–216.
- [14] Kathiravan, M. N.; Karthick, R.; Muthukumar, K. *Ex situ* bioremediation of Cr(VI) contaminated soil by *Bacillus* sp.: Batch and continuous studies. *Chem. Eng. J.* **2011**, *169*, 107–115.
- [15] Hu, B. W.; Song, Y. Z.; Wu, S. Y.; Zhu, Y. L.; Sheng, G. D. Slow released nutrient-immobilized biochar: A novel permeable reactive barrier filler for Cr(VI) removal. *J. Mol. Liq.* **2019**, *286*, 110876.
- [16] Acharya, R.; Naik, B.; Parida, K. Cr(VI) remediation from aqueous environment through modified-TiO₂-mediated photocatalytic reduction. *Beilstein J. Nanotechnol.* **2018**, *9*, 1448–1470.
- [17] Zhang, X.-J.; Ma, Y.-Y.; Bi, H.-X.; Yin, X.-Y.; Song, H.; Liu, M.-H.; Han, Z.-G. Wheel-shaped molybdenum(V) cobalt-phosphate cluster as a highly sensitive bifunctional photoelectrochemical sensor for the trace determination of Cr(VI) and tetracycline. *Inorg. Chem. Front* **2022**, *9*, 6457–6467.
- [18] Gu, Y. Q.; Li, Q.; Zang, D. J.; Huang, Y. C.; Yu, H.; Wei, Y. G. Light-induced efficient hydroxylation of benzene to phenol by quinolinium and polyoxovanadate-based supramolecular catalysts. *Angew. Chem., Int. Ed.* **2021**, *60*, 13310–13316.
- [19] Zhu, Y. T.; Huang, Y. C.; Li, Q.; Zang, D. J.; Gu, J.; Tang, Y. J.; Wei, Y. G. Polyoxometalate-based photoactive hybrid: Uncover the first crystal structure of covalently linked hexavanadate-porphyrin molecule. *Inorg. Chem.* **2020**, *59*, 2575–2583.
- [20] Li, X. Q.; Hong, Z.; Kang, S. Z.; Qin, L. X.; Li, G. D.; Mu, J. Photocatalytic degradation activity of TiO₂ nanotubes for Cr(VI). *Adv. Mater. Res* **2013**, *864–867*, 715–718.
- [21] Yuan, G. Q.; Li, F. L.; Li, K. Z.; Liu, J.; Li, J. Y.; Zhang, S. W.; Jia, Q. L.; Zhang, H. J. Research progress on photocatalytic reduction of Cr(VI) in polluted water. *Bull. Chem. Soc. Japan* **2021**, *94*, 1142–1155.
- [22] Bi, H. X.; Hou, L.; Yin, X. Y.; Ma, Y. Y.; Han, Z. G. Central metals to guide the bandgap of hourglass-type polyoxometalate hybrids as photocatalyst for the reduction of Cr(VI). *Cryst. Growth Des.* **2022**, *22*, 738–746.
- [23] Guo, H. L.; Wang, Y. K.; Qu, X. J.; Li, H. Y.; Yang, W.; Bai, Y.; Dang, D. B. Three-dimensional interpenetrating frameworks based on {P₄Mo₆} tetrameric clusters and filled with *in situ* generated alkyl viologens. *Inorg. Chem.* **2020**, *59*, 16430–16440.
- [24] Chen, C. R.; Zeng, H. Y.; Xu, S.; Shen, J. C.; Hu, G.; Zhu, R. L.; Du, J. Z.; Sun, Y. X. Facile fabrication of CdS/ZnAlO heterojunction with enhanced photocatalytic activity for Cr(VI) reduction under visible light. *Appl. Clay Sci.* **2018**, *165*, 197–204.
- [25] Wang, J. W.; Qiu, F. G.; Wang, P.; Ge, C. J.; Wang, C. C. Boosted bisphenol A and Cr(VI) cleanup over Z-scheme WO₃/MIL-100(Fe) composites under visible light. *J. Clean. Prod.* **2021**, *279*, 123408.
- [26] Wang, C. C.; Ren, X. Y.; Wang, P.; Chang, C. The state of the art review on photocatalytic Cr(VI) reduction over MOFs-based photocatalysts: From batch experiment to continuous operation. *Chemosphere* **2022**, *303*, 134949.
- [27] He, J.; Zhou, H. L.; Peng, Q. M.; Wang, Y. T.; Chen, Y. J.; Yan, Z. Y.; Wang, J. Q. UiO-66 with confined dyes for adsorption and visible-light photocatalytic reduction of aqueous Cr(VI). *Inorg. Chem. Commun.* **2022**, *140*, 109441.
- [28] Zhang, J. W.; Huang, Y. C.; Li, G.; Wei, Y. G. Recent advances in alkoxylation chemistry of polyoxometalates: From synthetic strategies, structural overviews to functional applications. *Coord. Chem. Rev.* **2019**, *378*, 395–414.
- [29] Li, J.; Zhang, D.; Chi, Y. N.; Hu, C. W. Catalytic application of polyoxovanadates in the selective oxidation of organic molecules. *Polyoxometalates* **2022**, *1*, 9140012.
- [30] Zhang, H. Y.; Zhao, W. L.; Li, H. Q.; Zhuang, Q. H.; Sun, Z. Q.; Cui, D. Y.; Chen, X. J.; Guo, A.; Ji, X.; An, S. et al. Latest progress in covalently modified polyoxometalates-based molecular assemblies and advanced materials. *Polyoxometalates* **2022**, *1*, 9140011.
- [31] Shi, J. Y.; Gupta, R. K.; Deng, Y. K.; Sun, D.; Wang, Z. Recent advances in the asymmetrical templation effect of polyoxometalate in silver clusters. *Polyoxometalates* **2022**, *1*, 9140010.
- [32] Li, L.; Zhao, Y.; Wang, J. J.; Chen, H. H.; Li, H. Y.; Wang, J. J.; Wang, Y. Y.; Bai, Y.; Dang, D. B. The [Cu₄Cl₄] cluster of a coordination complex based on polypyridyl ligand for heterogeneous Fenton-like MB degradation without illumination and electrocatalytic reduction of H₂O₂ and K₂Cr₂O₇. *Dyes Pigm.* **2022**, *207*, 110763.
- [33] Xing, X. X.; Guo, H. L.; He, T. M.; An, X.; Li, H. P.; Zhu, W. S.; Li, H. M.; Pang, J. Y.; Dang, D. B.; Bai, Y. Tungstovanadate-based ionic liquid catalyst [C₂(MIM)₂]₂VW₁₂O₄₀ used in deep desulfurization for ultraclean fuel with simultaneous recovery of the sulfone product. *ACS Sustainable Chem. Eng.* **2022**, *10*, 11533–11543.
- [34] Li, H. Y.; Pan, H.; Fan, Y. H.; Bai, Y.; Dang, D. B. Syntheses, crystal structures, and properties of four polyoxometalate-based metal-organic frameworks based on Ag(I) and 4,4'-dipyridine-N,N'-dioxide. *Polyoxometalates* **2022**, *1*, 9140007.
- [35] Yin, X. Y.; Zhang, Y. Q.; Ma, Y. Y.; He, J. Y.; Song, H.; Han, Z. G. Bifunctional sensors based on phosphomolybdates for detection of inorganic hexavalent chromium and organic tetracycline. *Inorg. Chem.* **2022**, *61*, 13174–13183.
- [36] Benseghir, Y.; Solé-Daura, A.; Mialane, P.; Marrot, J.; Dalecky, L.; Béchu, S.; Frégnaux, M.; Gomez-Mingot, M.; Fontecave, M.; Mellot-Draznieks, C. et al. Understanding the photocatalytic reduction of CO₂ with heterometallic molybdenum(V) phosphate polyoxometalates in aqueous media. *ACS Catal.* **2022**, *12*, 453–464.
- [37] Du, J.; Ma, Y. Y.; Xin, X.; Na, H.; Zhao, Y. N.; Tan, H. Q.; Han, Z.

- G.; Li, Y. G.; Kang, Z. H. Reduced polyoxometalates and bipyridine ruthenium complex forming a tunable photocatalytic system for high efficient CO₂ reduction. *Chem. Eng. J.* **2020**, *398*, 125518.
- [38] Zhu, W.; Yang, X. Y.; Li, Y. H.; Li, J. P.; Wu, D.; Gao, Y.; Yi, F. Y. A novel porous molybdophosphate-based Fe^{III}-MOF showing selective dye degradation as a recyclable photocatalyst. *Inorg. Chem. Commun.* **2014**, *49*, 159–162.
- [39] Zhang, Y. Q.; Zhou, L. Y.; Ma, Y. Y.; Dastafkan, K.; Zhao, C.; Wang, L. Z.; Han, Z. G. Stable monovalent aluminum(I) in a reduced phosphomolybdate cluster as an active acid catalyst. *Chem. Sci.* **2021**, *12*, 1886–1890.
- [40] Lin, B. Z.; Liu, X. Z.; Xu, B. H.; Wang, Q. Q.; Xiao, Z. J. Two new molybdenum(V) phosphates containing sandwich-shaped clusters with zero- and three-dimensional structures. *Solid State Sci.* **2008**, *10*, 1517–1524.
- [41] Niu, J. Q.; An, W. T.; Zhang, X. J.; Ma, Y. Y.; Han, Z. G. Ultra-trace determination of hexavalent chromium in a wide pH range triggered by heterometallic Cu-Mn centers modified reduced phosphomolybdate hybrids. *Chem. Eng. J.* **2021**, *418*, 129408.
- [42] Hou, L.; Zhang, Y. Q.; Ma, Y. Y.; Wang, Y. L.; Hu, Z. F.; Gao, Y. Z.; Han, Z. G. Reduced phosphomolybdate hybrids as efficient visible-light photocatalysts for Cr(VI) reduction. *Inorg. Chem.* **2019**, *58*, 16667–16675.
- [43] Han, L.; Zhong, Y. L.; Su, Y.; Wang, L. T.; Zhu, L. S.; Fei, X. F.; Dong, Y. Z.; Hong, G.; Zhou, Y. T.; Fang, D. Nanocomposites based on 3D macroporous biomass carbon with SnS₂ nanosheets hierarchical structure for efficient removal of hexavalent chromium. *Chem. Eng. J.* **2019**, *369*, 1138–1149.
- [44] Shi, H. F.; Yu, Y. C.; Zhang, Y.; Feng, X. J.; Zhao, X. Y.; Tan, H. Q.; Khan, S. U.; Li, Y. G.; Wang, E. B. Polyoxometalate/TiO₂/Ag composite nanofibers with enhanced photocatalytic performance under visible light. *Appl. Catal. B: Environ.* **2018**, *221*, 280–289.
- [45] Gan, H. H.; Liu, J.; Zhang, H. N.; Qian, Y. X.; Jin, H. X.; Zhang, K. F. Enhanced photocatalytic removal of hexavalent chromium and organic dye from aqueous solution by hybrid bismuth titanate Bi₄Ti₃O₁₂/Bi₂Ti₂O₇. *Res. Chem. Intermed.* **2018**, *44*, 2123–2138.
- [46] Bi, H. X.; Yin, X. Y.; Zhang, X. J.; Ma, Y. Y.; Han, Z. G. Efficient visible-light-driven reduction of hexavalent chromium catalyzed by conjugated organic species modified hourglass-type phosphomolybdate hybrids. *CrystEngComm* **2022**, *24*, 1002–1009.
- [47] Arslanoğlu, H.; Altundoğan, H. S.; Tümen, F. Photocatalytic reduction of Cr(VI) from aqueous solutions with formic acid in the presence of bauxite: kinetics and mechanism. *Trans. Indian Inst. Met.* **2021**, *74*, 3075–3084.
- [48] Liu, C. X.; Fang, W. C.; Song, Y. T.; Li, F. Y.; Sun, Z. X.; Xu, L. Fabrication of CdS/P₂Mo_xW_{18-x} nanospheres with type II heterostructure for photocatalytic reduction of hexavalent chromium. *Mater. Sci. Semicond. Process.* **2020**, *120*, 105276.



Xiao-Yu Yin is currently pursuing a MCs degree under the guidance of Prof. Zhangang Han from Hebei Normal University, China. Her current research interests are mainly focused on photoelectrochemical investigation of polyoxometalate-based materials.



Jing-Yan He is currently pursuing a MCs degree under the guidance of Prof. Zhangang Han from Hebei Normal University, China. Her current research interests are mainly focused on photocatalysis investigation of polyoxometalate-based materials.



Hao-Xue Bi is currently pursuing a Ph.D. degree under the guidance of Prof. Zhangang Han from Hebei Normal University, China. Her current research interests are mainly focused on photochemical investigation of polyoxometalate-based materials.



Yuan-Yuan Ma received her Ph.D. degree from Northeast China Normal University in 2018. She was introduced as a third-level talent by Hebei Normal University in China in the same year. Her current research interests are focused on the functionalization of polyoxometalate based materials.



Hao Song is currently pursuing a MCs degree under the guidance of Prof. Zhangang Han from Hebei Normal University, China. Her current research interests are mainly focused on electrochemical investigation of polyoxometalate-based materials.



Ting-Ting Fang is currently pursuing a Bachelor of Science degree at Hebei Normal University, China. She is working on the “the undergraduate innovation and entrepreneurship training program” by Prof. Zhangang Han.



Zhan-Gang Han received his Ph.D. degree from Northeast Normal University in 2005. In 2010–2011, he worked as a university teacher-visiting scholar at two universities in Monash University and The University of New South Wales, Australia. His current research interests focus on the construction of novel polyoxometalate structures and their photo-electrochemistry research. In 2016, he was funded by the Outstanding Youth Fund of Hebei Province and was selected as the third-level candidate for the “Three-Three-Three Talents Project” in Hebei Province. He has published more than 100 papers in important international academic journals. He presided over and completed a number of national and provincial natural science fund research projects; in 2013, he won the third prize of the Natural Science of Hebei Province.